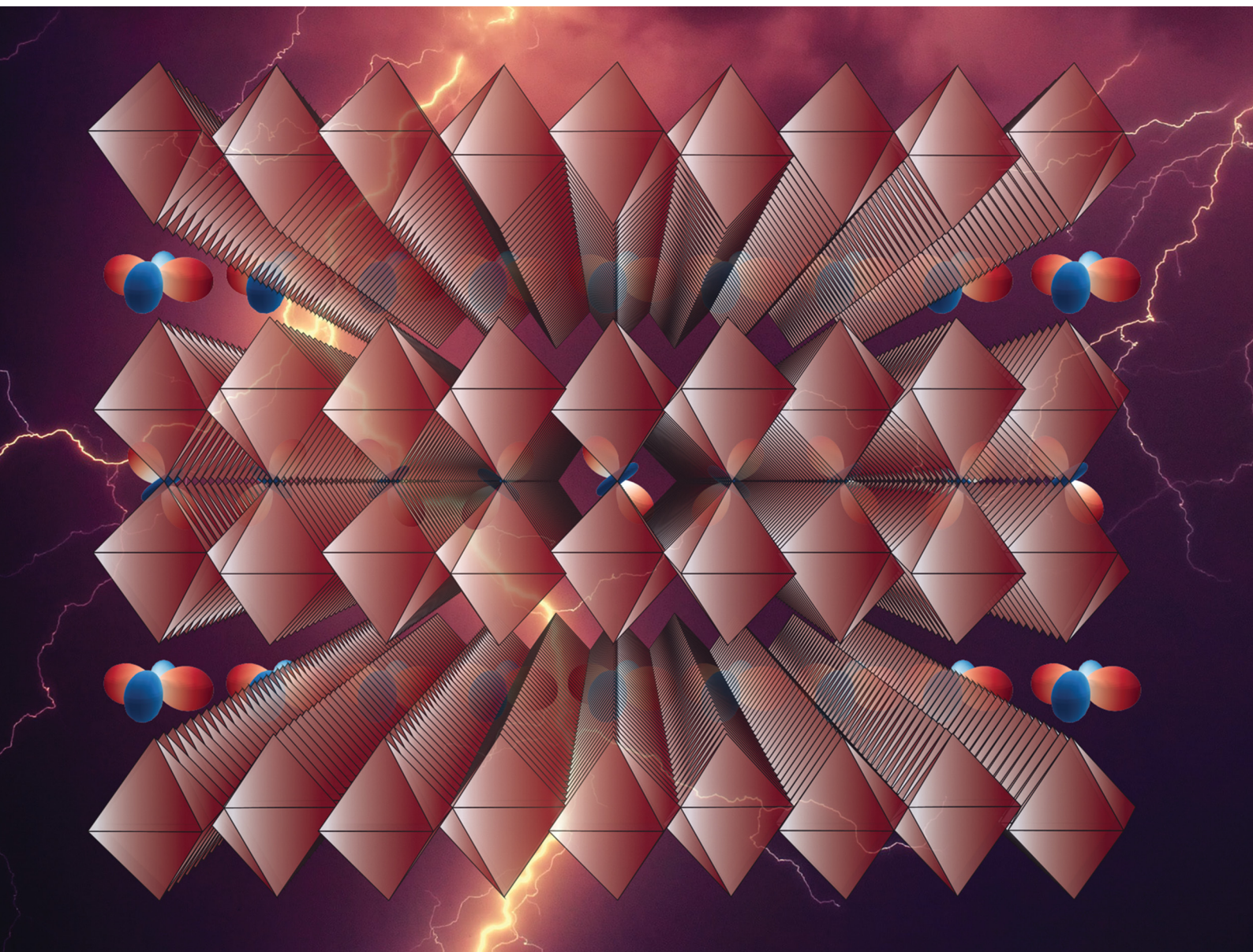


Journal of Materials Chemistry C

Materials for optical, magnetic and electronic devices

rsc.li/materials-c










ISSN 2050-7526

PAPER

Samuel S. M. Santos *et al.*
Spontaneous electric polarization and electric field gradient
in hybrid improper ferroelectrics: insights and correlations

PAPER

[View Article Online](#)
[View Journal](#) | [View Issue](#)Cite this: *J. Mater. Chem. C*, 2021,
9, 7005Spontaneous electric polarization and electric
field gradient in hybrid improper ferroelectrics:
insights and correlations†Samuel S. M. Santos, ^a Michel L. Marcondes, ^b Ivan P. Miranda, ^b
Pedro Rocha-Rodrigues,^a Lucy V. C. Assali, ^b Armandina M. L. Lopes, ^a
Helena M. Petrilli ^b and Joao P. Araujo ^a

An *ab initio* study of several hybrid improper ferroelectric (HIF) materials in the Ruddlesden–Popper phases and double perovskite structures is here presented. The focus is on the correlation between the electric field gradient at several nuclear sites (EFG) and the spontaneous electric polarization. As observed in some proper ferroelectrics, we found that the EFG tensor components, along possible switching paths to invert the polarization, are interchangeable between the ferroelectric and paraelectric phases in the HIF $AA_2'B_2O_7$ and $AA'B_2O_6$ ($A, A' = \text{Ca, Cd}$ and $B = \text{Mn, Ti}$) compounds. The results indicate that the relationship between the main continuous component of the EFG tensor and the electric polarization, even at sites without inversion symmetry, is primarily quadratic. Moreover, the claimed linear correlation was not observed. These results open a route to analyze the local octahedral distortions that underline HIF materials' functional multiferroic properties.

Received 2nd March 2021,
Accepted 29th April 2021

DOI: 10.1039/d1tc00989c

rsc.li/materials-c

1 Introduction

The short-range interaction and high sensitivity to atomic positions make hyperfine interactions capable of evaluating local parameters of crystals with high precision. Experiments such as perturbed angular correlation (PAC) spectroscopy, nuclear magnetic resonance (NMR), and nuclear quadrupole resonance (NQR) have measured the electric field gradient at the nucleus (EFG) and provided a large amount of detailed information at the atomic scale of several types of systems.^{1,2} Whereas hyperfine interactions are susceptible to the atomic order, experimental measurements of the EFG are useful in studying distortions responsible for ferroelectric phase transitions.³ On the other hand, these distortions generate a spontaneous electric polarization (P). Therefore, the relationship between P and the EFG tensor can be suitable for analyzing experimental results to understand these transitions. In particular, this information can be relevant to determine/confirm the existence of ferroelectric phases in systems whose experimental

evidence of such phases does not exist. In these systems, experimental signatures of ferroelectric order can be veiled due to high electric leakage currents that inhibit polarization measurements,⁴ or due to the limitations of crystallographic approaches based on long-range average models, that have a low sensitivity to discern between low and high symmetry structures.^{5,6}

Several experimental studies have explored the relationship between P and the EFG components, which provide details of the electronic charge distribution around an atomic site. The first-order quadrupole splitting has been used to measure P of the ferroelectric Rochelle salt,^{7–9} at which the quadrupole splitting is proportional to P .¹⁰ The first-order quadrupole splitting in NMR is a linear function of the nuclear quadrupole moment and the EFG components, enabling the study of the relationship between EFG and P . Dening and Casabella¹⁰ used the Taylor expansion of the EFG w.r.t. atomic distortions to show that, if the paraelectric phase possesses inversion symmetry at the EFG site, the linear term vanishes and the relationship between EFG and P is quadratic. In general, the EFG is expected to be proportional to P unless the atoms sit at positions with inversion symmetry, in which case the EFG is proportional to P^2 .¹⁰ The quadratic relationship was also demonstrated for PbHfO_3 ¹¹ and BaTiO_3 .¹² Additionally, PAC measurements have also studied ferroelectric phase transitions in charge ordered manganites through changes in the EFG tensor.¹³

^a IFIMUP, Institute of Physics for Advanced Materials,
Nanotechnology and Photonics, Departamento de Física e Astronomia da
Faculdade de Ciências da Universidade do Porto, Rua do Campo Alegre,
687 4169-007, Porto, Portugal. E-mail: samucafisica@gmail.com

^b Universidade de São Paulo, Instituto de Física, Rua do Matão, 1371, 05508-090,
São Paulo, SP, Brazil

† Electronic supplementary information (ESI) available. See DOI: 10.1039/d1tc00989c

From a theoretical perspective, density functional theory (DFT) has been an important tool in predicting the EFG parameters.¹⁴ Recently, an *ab initio* study observed a quadratic dependence between P and EFG in proper perovskite ferroelectric materials.¹⁵ The exceptions were PbTiO_3 and CaTiO_3 that required quartic terms in the EFG expansion to properly fit the data. Although the EFG tensor remained continuous in such cases, the oxygen atoms at the equatorial sites of the octahedron exhibited discontinuous variations of the EFG components w.r.t. P . Additionally, hyperfine parameters obtained by first principles calculations have provided supplementary information about the different origins of the ferroelectric states in YMnO_3 and YMn_2O_5 compounds.¹⁶

Combining PAC spectroscopy with DFT calculations, Gonçalves *et al.* showed that the largest component of the EFG tensor, V_{zz} , is almost insensitive to the polarization changes in $\text{Sr}_{0.5}\text{Ba}_{0.5}\text{MnO}_3$, which is a system based on the alkaline-earth manganites.¹⁷ In this multiferroic compound, the trend of V_{zz} with P does not follow the rule suggested by Dening and Casabella.¹⁰ The association of these two techniques to obtain the connection between EFG and P has also been used to characterize the ferroelectric states of rare-earth orthochromites, assisting in understanding the ferroelectric behaviour of the SmCrO_3 system.¹⁸ Complementarily, DFT has also been used to calculate the EFG tensor in trichloroacetyl halides, showing that it is a powerful method for predicting electronic states prior to accomplishing experiments.¹⁹

In addition to the materials already discussed, there are other ferroelectric materials where the ferroelectric state is reached by complex inversion symmetry breaking mechanisms. In hybrid improper ferroelectric (HIF) systems, such as Ruddlesden–Popper (RP) and double perovskite (DP) structures, the transition to a ferroelectric state is driven by two oxygen octahedral distortions, which enable a polar displacement. Whereas the EFG provides detailed information on the electronic charge distribution around an atomic site, hyperfine techniques such as NQR/NMR or PAC spectroscopy are interesting techniques to study HIF phase transitions.⁵ However, the trilinear coupling in HIF materials happens *via* a large set of atomic distortions, and it is still not clear how P varies with the EFG. On the other hand, DFT has been a powerful formalism for predicting electronic, structural, magnetic, and vibrational properties of materials. Therefore, here we use the DFT technique to unravel the relationships between the EFG tensor and the spontaneous electric polarization in complex HIF perovskites with the RP phase and the DP structures, that have the general formulae $\text{AA}_2'\text{B}_2\text{O}_7$ and $\text{AA}'\text{B}_2\text{O}_6$, respectively, where A, A' = Ca, Cd and B = Mn, Ti.

This work is organized as follows. In Section 2, we present the methodology and the computational details used in this investigation. In Section 3, we present and discuss the results and the relationship between P and EFG components for the HIF systems, for each chemical element and atomic site. Finally, in Section 4, we draw our conclusions.

2 Methodology

The electronic calculations were performed within the framework of the DFT in the Kohn–Sham scheme, with the Perdew–Burke–Ernzerhof (PBE) GGA exchange–correlation potential,²⁰ as implemented in the Quantum ESPRESSO computational package.^{21,22} The electronic wave functions were treated using the projected augmented wave (PAW) method,²³ and the primitive cell parameters were optimized for null pressure by the variable cell shape molecular dynamics method.^{24,25} The electric polarization was calculated through the modern theory of polarization.^{26,27} The plane-wave basis was arranged for a cut-off energy of 110 Ry and each Brillouin zone was sampled by a $7 \times 4 \times 4$ k -mesh, following the Monkhorst–Pack scheme.²⁸ For the Mn-related magnetic systems, we searched for the ground state by performing calculations for ferromagnetic and anti-ferromagnetic alignments. The magnetic ground state is G-type antiferromagnetic (AFM-G) for $\text{Ca}_3\text{Mn}_2\text{O}_7$, $\text{CaCd}_2\text{Mn}_2\text{O}_7$, and $\text{CaCdMn}_2\text{O}_6$ and C-type antiferromagnetic (AFM-C) for $\text{Cd}_3\text{Mn}_2\text{O}_7$.²⁹ Although spin–orbit coupling (SOC) can change important aspects of ferroelectric perovskites, for instance giving rise to exotic spin-splitting phenomena,^{30–35} the properties of interest (*i.e.* EFG and P) in the materials studied here are not significantly affected by SOC, even with the presence of cadmium.^{5,29} Furthermore, the inclusion of Hubbard U correction in these Mn-based systems also does not have a large effect on these properties.^{5,29} Therefore, it was not necessary to use SOC or Hubbard U correction in this work.

RP2 phases are layered compounds with the chemical formula $\text{AA}_2'\text{B}_2\text{O}_7$ and DP structures are superlattice compounds with the formula $\text{AA}'\text{B}_2\text{O}_6$. In both systems, the A- and A'-sites can be occupied by Ca or Cd atoms and the B-site by Mn or Ti atoms. In the RP2 perovskites, when $A = A'$, the systems correspond to the pristine RP2 phases: $\text{Ca}_3\text{B}_2\text{O}_7$ and $\text{Cd}_3\text{B}_2\text{O}_7$. When $A \neq A'$, the structure corresponds to $\text{CaCd}_2\text{B}_2\text{O}_7$. The A- and A'-sites in RP2 are given special names, perovskite site (pv-site) and rocksalt site (rs-site), respectively.

The HIF mechanism is present in both systems, the RP2 perovskites and DP structures.²⁹ Experiments confirmed that, at high temperatures, the RP2 structure belongs to the $I4/mmm$ (#139) centrosymmetric space group.⁵ As the temperature decreases, the system undergoes a phase transition to the $A2_1am$ (#36) space group. The centrosymmetric DP structure belongs to the $Cmmm$ (#65) space group and the non-centrosymmetric phase to the $Pmc2_1$ (#26) one.²⁹

In these systems, two soft phonon modes drive the phase transition in both structures: for RP2 crystals the direct transformation $I4/mmm \rightarrow A2_1am$ comprises a rotation followed by a tilt that transforms according to X_2^+ and X_3^- irreducible representations (IRs), respectively, while for the DP structures, similarly, the direct transition $Cmmm \rightarrow Pmc2_1$ transforms as Y_2^+ and Y_3^- IRs. Together, X_2^+ and X_3^- (Y_2^+ and Y_3^-) distortions enable a polar displacement transforming as the Γ_5^- (Γ_4^-) IR. Because three distortion modes relate the $I4/mmm$ ($Cmmm$) to the $A2_1am$ ($Pmc2_1$) space groups, the free energy expansion has a trilinear coupling term:

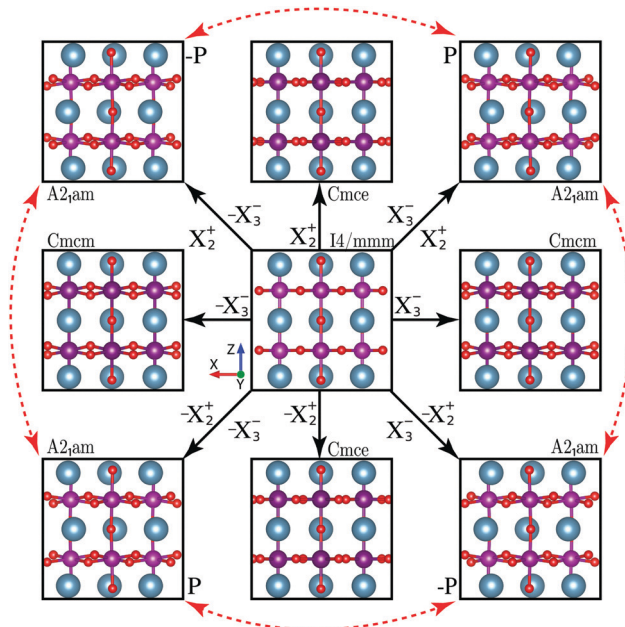


Fig. 1 Relationship between the parent $I4/mmm$ and the $A2_1am$ space groups, together with the twin images for the two possible switching paths to invert the sign of the spontaneous electric polarization (see text).

$$F \propto aQ_1Q_2Q_3 \quad (1)$$

where depending on whether the phase is RP2 or DP, Q_1 is X_2^+ or Y_2^+ , Q_2 is X_3^- or Y_3^- , and Q_3 is Γ_5^- or Γ_4^- .

To study the relationship between spontaneous P and the EFG components, we used the ISOTROPY software suite^{36,37} and applied several distortions to invert Q_1 and Q_2 IRs and, for each distortion, P and EFG components were computed. For the RP2 structures, i.e., the Γ_5^- distortion controls the polarization direction; thus to switch the polarization of the ferroelectric $A2_1am$ structure, this mode should be inverted. Therefore, because of the invariance of the free energy, eqn (1), the polarization sign switches by inverting X_2^+ or X_3^- , but not both.

Group theoretical methods predict, for the RP2 structures, eight structural domains for the phase transformation from $I4/mmm$ to $A2_1am$. Four of these domains correspond to origin shifts. From the remaining four, two maintain the same orientation of the Γ_5^- distortion, and two invert it. Therefore, two possible switching paths to invert the polarization exist. Fig. 1 illustrates these mechanisms, showing both switching paths. Starting from the parent $I4/mmm$ structure, one obtains the $A2_1am$ phase with both distortions, the rotation X_2^+ and the tilt X_3^- . The Γ_5^- distortion corresponds to the displacement of the blue spheres (Ca atoms) along the x direction. At the $I4/mmm$ space group, the Ca atoms are sited at centrosymmetric positions; thus, the total polarization is null. Upon the Γ_5^- distortion, Ca atoms displace along the x axis and the polarization emerges.

Starting from the polar $A2_1am$ structures, inverting X_2^+ or X_3^- will also invert the orientation of the Ca atoms' displacement, therefore switching the polarization (dashed red arrows

in Fig. 1). The inversion of the X_2^+ distortion, starting from the $A2_1am$ phase, results in the $Cmcm$ intermediate centrosymmetric phase when the X_2^+ and Γ_5^- distortions both become null and only X_3^- is active. When X_3^- is inverted, the intermediate centrosymmetric structure is $Cmce$.

In the following discussion, the set of intermediate structures between the $Cmcm$ and $A2_1am$ phases will be called the X_2^+ path, shown as vertical dashed red arrows in Fig. 1. Analogously, the path between $Cmce$ and $A2_1am$ will be called the X_3^- path, shown as horizontal dashed red arrows in Fig. 1. The relationships between the $Cmmm$ and $Pmc2_1$ intermediate space groups of the DP structures are similar to those of RP2 phases described above. In this case, the intermediate centrosymmetric structures are $Pmma$ (#51) and $Pbam$ (#55). The path between $Pmma$ and $Pmc2_1$ will be called the Y_2^+ path, and between $Pbam$ and $Pmc2_1$ the Y_3^- path.

EFG is a local property that is heavily influenced by the local order at the atomic site. Therefore, the EFG at a specific nucleus site in perovskites reflects the octahedral rotation variations and the atomic displacements. Because the local order is different along the X_2^+ and X_3^- (Y_2^+ and Y_3^-) paths, the EFG is a helpful indicator of the ferroelectric transition paths in the HIF perovskites. The EFG is a symmetric tensor with V_{xx} , V_{yy} and V_{zz} being the diagonal elements. In the principal system of axes we have $V_{xx} + V_{yy} + V_{zz} = 0$ and, conventionally, these components are chosen such that $|V_{zz}| \geq |V_{yy}| \geq |V_{xx}|$. Instead of specifying three diagonal elements, usually V_{zz} (the largest component of the EFG tensor) and the asymmetry parameter $\eta = (V_{xx} - V_{yy})/V_{zz}$ are reported.

To describe and analyze the EFG tensor components, we followed the approach of ref. 38, which provides a way to visualize the EFG principal components through a graphical representation w.r.t. the atom crystalline environment. Thereby, we write a function, with the origin at an atom, as

$$f = r^2 g(\theta, \phi), \quad (2)$$

where $g(\theta, \phi)$ is a polar function whose surfaces represent angular variations of the EFG tensor components.

3 Results

The variations of the EFG tensor components of the $\text{Ca}_3\text{Mn}_2\text{O}_7$ compound, along both ferroelectric transition paths displayed in Fig. 1, were computed by using the methodology described in the previous section. Fig. 2 shows the computed $g(\theta, \phi)$ surface with the origin at Ca atoms at pv- and rs-sites and at Mn atoms, for the four phases shown in Fig. 1, along X_2^+ and X_3^- paths. The $g(\theta, \phi)$ surface of other RP2 can be found in the ESI.†

Within the adopted procedure, the polar function plot shape that resembles a d_{z^2} atomic orbital, as shown in Fig. 2(a) for example, characterizes an EFG with a small asymmetry parameter η , while the surface shape that resembles a $d_{z^2-y^2}$ atomic orbital, as in Fig. 2(b), is characteristic of an EFG with a large η . Additionally, in Fig. 2(g), the asymmetry parameter η has an

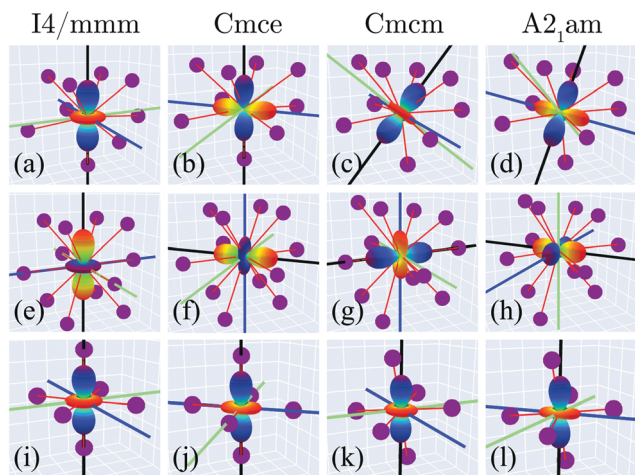


Fig. 2 $g(\theta, \phi)$ surface plot of the $\text{Ca}_3\text{Mn}_2\text{O}_7$ compound for the parent centrosymmetric $I4/mmm$, polar $A2_1am$, and the centrosymmetric $Cmcm$ and $Cmce$ space groups along the X_2^+ and X_3^- paths, respectively. (a–d) At Ca rs-site (A' -site), (e–h) at Ca pv-site (A -site), and (i–l) at Mn-site (B -site). The green, blue, and black axes represent the directions of the V_{xx} , V_{yy} , and V_{zz} EFG components, respectively. The blue regions depict where the polar function is negative and the red regions where it is positive. The coordinated axes of the crystal were defined based on the MnO_6 octahedron in the parent centrosymmetric $I4/mmm$ phase, on the frame (i), as follows: the z -axis is defined by the apical oxygen atoms and the xy -plane by the equatorial oxygen atoms.

intermediate value, about 0.4, which is indicated by the distorted surface shape of the polar function negative region. More information about the asymmetry parameter can be found in the ESI.†

Since the octahedral rotations of the oxygen cages slightly modify the local symmetry around the Mn ion, the effect of this distortion on η is small, *i.e.*, η values always remain close to zero, as shown in Fig. 2(i–l). In this site, the V_{zz} component is always parallel to the z -axis for all space groups. In general, the tilt and rotation modes do not change the direction of V_{zz} , but they change the other two components. In addition, the V_{zz}

component at the Mn site is always negative. In the $Cmce$ space group, although the MnO_6 octahedra rotate only 8.7° , the EFGs rotate 51.4° around the z -axis, w.r.t. the lattice vectors. For the $Cmcm$ space group, the MnO_6 octahedra tilt about 9.7° around the xy -plane, and the V_{zz} components tilt less than 1° . Although the octahedra undergo an inclination in this last phase, the V_{zz} component does not follow this inclination. Because the rotation around the z -axis is null, the V_{xx} and V_{yy} principal axes have similar directions to those of the $I4/mmm$ structure. In the polar $A2_1am$ ground state, Fig. 2(l), the oxygen octahedra are distorted w.r.t. the parent $I4/mmm$ structure *via* both the tilt and the rotation distortions. Thereby, both effects are present and an axis rotation in the x and y directions exists, alongside a small shift of the z -axis.

Fig. 2(a–d) and (e–h) show the EFG components on the Ca atoms at rs- and pv-sites, respectively. The large deformation of the atoms surrounding these sites causes large variations in the η parameter, affecting the shape of the surfaces. The Ca atoms at pv-sites (A -site) have a small η in the $Cmcm$ and $I4/mmm$ space groups, Fig. 2(e) and (f), but a large one in the $A2_1am$ structure, Fig. 2(h), and an intermediate one in the $Cmce$, Fig. 2(g). The Ca atoms at rs-sites (A' -site) have a different behaviour in the structure $Cmce$; here η is large, Fig. 2(b). η remains close to 1 in the $A2_1am$ structure, Fig. 2(d), and becomes zero in the $Cmcm$ structure, Fig. 2(c). Because of the conventional ordering of the EFG components ($|V_{zz}| \geq |V_{yy}| \geq |V_{xx}|$), the orientation of the conventional principal axes may change not only due to the evolutions of the neighboring octahedral distortions, but also due to the conventional ordering, that defines the V_{zz} , V_{yy} , V_{xx} EFG components, according to the mathematical relation $|V_{zz}| \geq |V_{yy}| \geq |V_{xx}|$; such a swap of the EFG components can occur, specifically, when the asymmetry parameter approaches the extreme values, of $\eta \approx 0$ (V_{xx} for V_{yy} , *vice versa*) or $\eta \approx 1$ (V_{zz} for V_{yy} , *vice versa*). Fig. 2(g) shows the V_{yy} component pointing in the z -axis direction, while in Fig. 2(h) it is the V_{xx} component that points towards the z -axis. Clearly, interchanges occur between the V_{xx} and V_{yy} principal axes. To compare the variations of the EFG components among the several structures, these interchanges must be

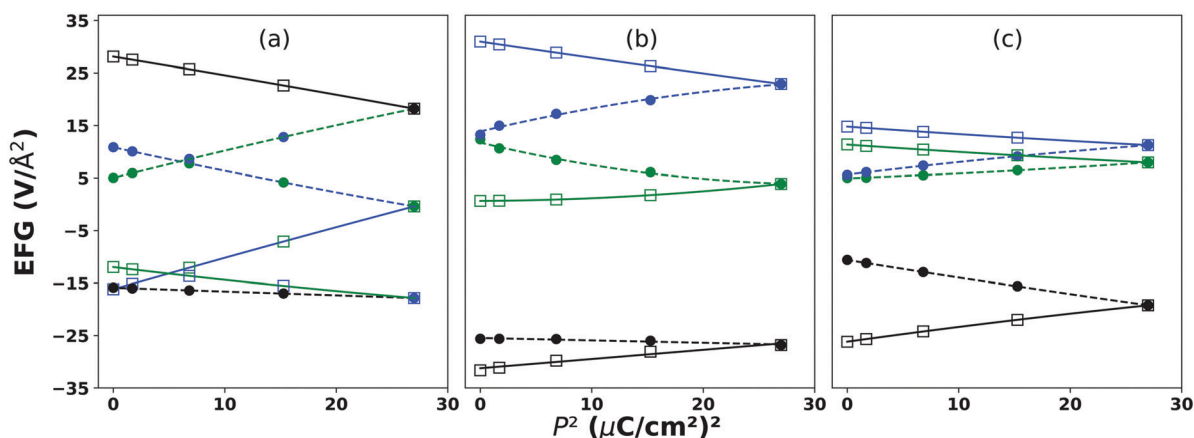


Fig. 3 Electric field gradient (EFG) components versus the spontaneous polarization squared (P^2) for $\text{Ca}_3\text{Mn}_2\text{O}_7$: (a) at Ca pv-site (A -site); (b) at Ca rs-site (A' -site); (c) at Mn-site (B -site). The symbols refer to the EFG components in each path X_2^+ and X_3^- as follows: ● $V_{xx}(X_2^+)$, ● $V_{yy}(X_2^+)$, ● $V_{zz}(X_2^+)$, □ $V_{xx}(X_3^-)$, □ $V_{yy}(X_3^-)$, □ $V_{zz}(X_3^-)$. The lines refer to the alternative EFG components in the X_2^+ and X_3^- paths as follows: --- $V_1(X_2^+)$, --- $V_2(X_2^+)$, --- $V_3(X_2^+)$, --- $V_1(X_3^-)$, --- $V_2(X_3^-)$, --- $V_3(X_3^-)$.

taken into account, since they do not correspond to physical variations on the EFG components due to the distortions, but to an alteration in the coordinate system of the EFG tensor principal axes, due to the conventional mathematical ordering. Therefore, to explore the relationship between P and EFG, the changes in the principal axes of the EFG tensor, along the distortion paths, have to be understood. To illustrate this, Fig. 3 shows the EFG components *versus* P^2 for the $\text{Ca}_3\text{Mn}_2\text{O}_7$ compound at Ca and Mn sites, where coloured filled circles and empty squares represent the EFG components along X_2^+ and X_3^- paths, respectively.

Interchanges between the EFG components at Ca pv-sites may be easily noted in Fig. 3(a). When fitting the data, linking the EFG component values from the initial centrosymmetric Cmcm or Cmce structures, where $P = 0$, to the final polar $\text{A2}_1\text{am}$ structure, where $P = 5.19 \mu\text{C cm}^{-2}$, there are interchanges between the EFG components, provided that a specific line fits data that have different colored symbols; otherwise no interchange occurs. For example, the blue dashed line, in Fig. 3(a), connects a green circle to a black circle, demonstrating a $V_{xx} \rightarrow V_{zz}$ interchange in the transition from the apolar to the polar phase along the X_2^+ path. In this path there are two more interchanges: $V_{yy} \rightarrow V_{xx}$ and $V_{zz} \rightarrow V_{yy}$. For the X_3^- path the interchanges are $V_{xx} \rightarrow V_{yy}$ and $V_{yy} \rightarrow V_{xx}$. Fig. 3(b) and (c) indicate that no interchanges occur at the Ca rs-site and Mn-site.

Interchanges between EFG components, at some atomic site, have been observed for the PbTiO_3 and CaTiO_3 proper ferroelectrics,¹⁵ just like what we found here for the $\text{Ca}_3\text{Mn}_2\text{O}_7$ crystal at the Ca pv-site, Fig. 3(a). This behaviour makes describing the variations of the EFG components in terms of its largest component, V_{zz} , inappropriate. Fig. 3(a), symbol marks, shows that, due to the standard definition of the EFG tensor, some variations of its components are discontinuous, as V_{xx} and V_{yy} in both X_2^+ and X_3^- paths, and V_{zz} in the X_2^+ path. However, the adjusted lines show that the EFG tensor is continuous. Thus, here we will describe the variation of the EFG tensor through an alternative component, which will be called V_3 , that corresponds to the EFG V_{zz} component of the undistorted phase. If there are no interchanges, as in Fig. 3(b) and (c), the V_3 component is always the same as V_{zz} ; otherwise, as in Fig. 3(a), V_3 might be V_{xx} or V_{yy} in the distorted phase. Therefore, in Fig. 3, V_3 is represented by the black dashed and solid lines, along X_2^+ and X_3^- paths, respectively. Still in Fig. 3, the dashed and solid green and blue lines represent the V_1 and V_2 alternative components, in that sequence, along X_2^+ and X_3^- paths, respectively. These two components have the same definition as the V_3 one, but for V_{xx} and V_{yy} components instead of V_{zz} . Even with the complex atomic distortions in the HIF perovskites, P is a linear function of the atomic displacements,²⁹ that causes EFG variations at the nuclei sites. Since the atomic displacements $\delta\vec{r}$ are small, the EFG components can be expanded in a Taylor series:¹⁰

$$V_{zz} = V_{zz}^0 + e \sum_i \zeta_i \left[\left(\frac{3}{r_i^5} - \frac{15z_i^2}{r_i^7} \right) (x_i \delta x_i + y_i \delta y_i) + \left(\frac{9}{r_i^5} - \frac{15z_i^2}{r_i^7} \right) z_i \delta z_i \right], \quad (3)$$

where ζ_i is the number of electrons at site i , e is the electron charge, r_i is the distance between the atom i and the nucleus, and $\delta\mu_i$ is the component μ of the displacement $\delta\vec{r}$.

Fig. 3 shows that the EFG V_1 , V_2 , and V_3 alternative components of $\text{Ca}_3\text{Mn}_2\text{O}_7$ vary linearly with P^2 at almost all atomic sites, indicating that Taylor expansions up to second-order are suitable for fitting the data. We can notice a higher-order dependency of V_1 and V_2 components with the polarization only for the Ca atom at rs-site.

When inversion symmetry is present in the paraelectric structure, the linear terms vanish in the Taylor expansion.¹⁰ In the RP2 phases, only the cation pv-site of the Cmce undistorted phase along the X_3^- distortion path has inversion symmetry. This site is displayed by the solid black line in Fig. 3(a), where we observe a linear relationship between EFG and P^2 , as expected. However, the ferroelectricity in the HIF materials is due to a collection of atomic distortions. Therefore, it is supposed that high-order terms in the Taylor expansion should not be negligible for sites without inversion symmetry since the linear terms should prevail. However, most of the results obtained for all of the HIF materials based on the $\text{AA}_2'\text{B}_2\text{O}_7$ RP2 perovskites and $\text{AA}'\text{B}_2\text{O}_6$ DP structures, with A, A' = Ca, Cd; B = Mn, Ti, showed that Taylor expansion to second-order of the EFG is adequate, even for the complex atomic distortions of the studied systems. Only a few cases required fourth-order expansions. Using the expression $V_3(P) = V_3^0 + aP^2 + bP^4$ to fit the curves that relate the EFG and P , we show in Table 1 the values of the V_3^0 , a , and b coefficients for each of the RP2 and DP structures.

Fig. 4(a)–(c) show, respectively, the relationship between the EFG V_3 component and the standard deviation of the mean distance between an atomic site and its nearest neighbours (nn_std), the nn_std *versus* the spontaneous electric polarization P , and the nn_std *versus* the spontaneous electric polarization squared P^2 , for the $\text{Ca}_3\text{Mn}_2\text{O}_7$ compound, at Ca pv- and rs-sites and Mn-site, along the X_2^+ and X_3^- paths. The relationship between the V_3 component and the nn_std , Fig. 4(a), is linear and the relationship between nn_std and the spontaneous polarization is quadratic, Fig. 4(b) and (c). Therefore, the V_3 component has to be quadratic with the polarization at all sites of $\text{Ca}_3\text{Mn}_2\text{O}_7$. In general, for all systems studied here, we obtain that in the sites that have inversion symmetry, $V_3 \times \text{nn_std}$ has a linear relationship and $\text{nn_std} \times P$ has a quadratic one. Therefore, $V_3 \times P$ has a quadratic relationship, which agrees with the results obtained from the $V_3 \times P$ fit shown in Table 1. An exception here is the A'-site of the $\text{CaCdMn}_2\text{O}_6$ system, where a small quartic term had to be added to describe the $V_3 \times P$ relationship correctly. For the systems that do not have Cd atoms, $\text{Ca}_3\text{Mn}_2\text{O}_7$ and $\text{Ca}_3\text{Ti}_2\text{O}_7$, the behaviour of the $V_3 \times P$ relationship is the same for the sites with and without inversion symmetry. However, when Cd is present in the structure, this relationship is more complex and small quartic terms are needed to fit the data properly. Therefore, for most of the RP2 and DP sites, studying the relationship between the standard deviation of the mean distance of an atomic site and its nearest neighbours and EFG or P , we also found that the

Table 1 Values of the V_3^0 , a , and b coefficients for the fits of the expression $V_3(P) = V_3^0 + aP^2 + bP^4$, that relates the EFG component with P , for each of the RP2 and DP structures. V_3^0 and P are in units of $V \text{ \AA}^{-2}$ and $\mu\text{C cm}^{-2}$, respectively

System	Path	A-site			A'-site			B-site		
		V_3^0	a	b	V_3^0	a	b	V_3^0	a	b
$\text{Ca}_3\text{Mn}_2\text{O}_7$	X_2^+	-15.901	-0.071	0	-25.457	-0.046	0	-10.684	-0.318	0
	X_3^-	28.188	-0.368	0	-31.232	0.176	0	-26.039	0.256	0
$\text{Cd}_3\text{Mn}_2\text{O}_7$	X_2^+	-72.150	0.414	-0.002	-71.330	0.187	0	-11.551	-0.101	0
	X_3^-	-29.903	-0.255	0	82.404	-0.662	-0.005	-35.315	0.167	0
$\text{CaCd}_2\text{Mn}_2\text{O}_7$	X_2^+	-22.033	0.199	-0.003	-11.348	1.329	0	-9.550	-0.330	0
	X_3^-	39.687	-0.674	0	-103.061	2.874	-0.045	-21.389	-0.264	0.008
$\text{CaCdMn}_2\text{O}_6$	Y_2^+	-24.301	0.420	-0.011	-59.762	1.229	-0.038	9.369	-0.228	0
	Y_3^-	35.528	-1.055	0	69.353	-1.502	0	-7.739	-0.026	0.002
$\text{Ca}_3\text{Ti}_2\text{O}_7$	X_2^+	-24.969	0.004	0	-30.492	0.011	0	-14.161	-0.012	0
	X_3^-	28.559	-0.018	0	-54.153	0.049	0	-37.030	0.020	0
$\text{Cd}_3\text{Ti}_2\text{O}_7$	X_2^+	-82.051	0.006	0	93.952	-0.056	0.001	-17.349	-0.003	0
	X_3^-	86.944	-0.015	0	-153.211	0.064	0	-46.127	0.012	0
$\text{CaCd}_2\text{Ti}_2\text{O}_7$	X_2^+	-21.052	0.048	0	73.346	0.018	0	-9.895	-0.029	0
	X_3^-	42.053	-0.068	0	-127.526	0.197	0	-34.689	0.039	0
$\text{CaCdTi}_2\text{O}_6$	Y_2^+	-25.055	0.044	0	-76.639	0.020	0	3.559	-0.019	0
	Y_3^-	40.830	-0.054	0	74.279	-0.014	0	-24.459	0.029	0

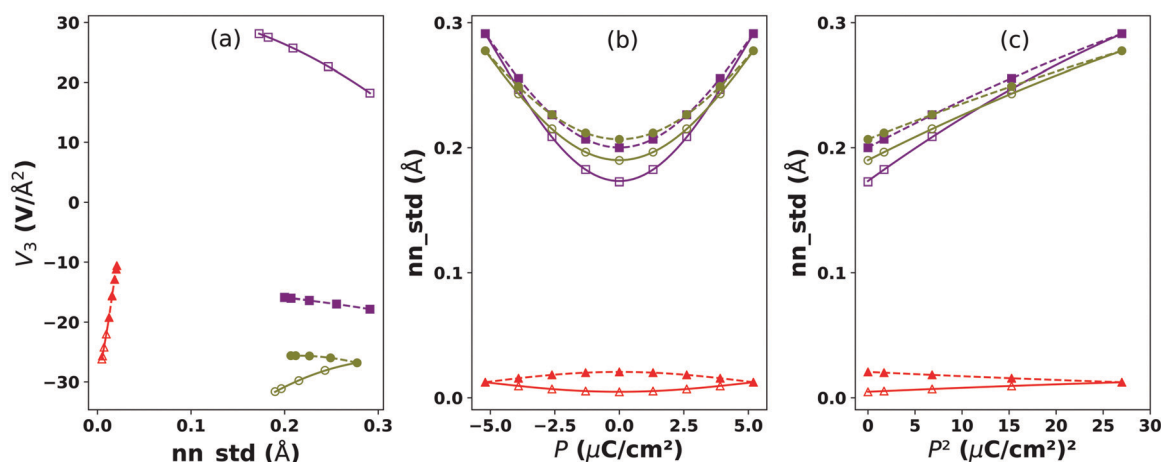


Fig. 4 (a) EFG V_3 component versus the standard deviation of the nearest neighbors' mean distance of an atomic site (nn_std); (b) nn_std versus the spontaneous electric polarization P ; (c) nn_std versus the spontaneous electric polarization squared P^2 for the $\text{Ca}_3\text{Mn}_2\text{O}_7$ compound at A-site (Ca pv-site, \blacksquare and \square), A'-site (Ca rs-site, \bullet and \circ), and B-site (Mn atom, \blacktriangle and \triangle). The dashed lines with filled symbols fit the data along the X_2^+ path, while the solid lines with empty symbols do it along the X_3^- path.

V_3 component is quadratic with the spontaneous electric polarization, and at some sites without inversion symmetry, small quartic terms are necessary to suitably fit the data.

Fig. 5 shows the relationship between the EFG V_3 component and the spontaneous electric polarization for all structures studied in this investigation and, in general, the majority of the sites of the RP2 and DP structures possess a quadratic dependence. However, at some sites of the systems where Cd is present, a small quartic term in the Taylor series is necessary to properly fit the data. The critical cases occur when the system

has Mn and Cd ions simultaneously, *i.e.*, in the $\text{Cd}_3\text{Mn}_2\text{O}_7$, $\text{CaCd}_2\text{Mn}_2\text{O}_7$, and $\text{CaCdMn}_2\text{O}_6$ compounds. On the other hand, for the Ti-based systems, only for Cd at the rs-site of the $\text{Cd}_3\text{Ti}_2\text{O}_7$ compound there was a need for the quartic term in the Taylor expansion to fit the data.

In Fig. 5, the red triangle marks correspond to the cations at the B-site of the $\text{AA}_2'\text{B}_2\text{O}_7$ (RP2) and $\text{AA}'\text{B}_2\text{O}_6$ (DP) structures, where A = Ca, A' = Cd, and B = Mn, Ti. The EFG V_3 component's behaviour with P , for these sites, is opposite in both distortion path directions: it is convex along the X_3^- distortion path and

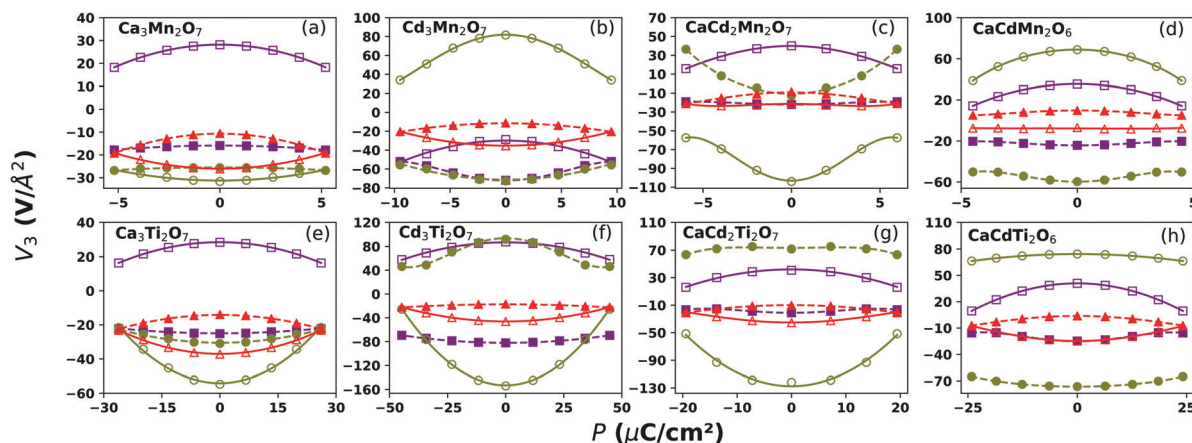


Fig. 5 EFG V_3 component versus the spontaneous electric polarization P for the RP2 and DP structures. A-site (■ and □), A'-site (● and ○), and B-site (▲ and △). The dashed lines with filled symbols correspond to the X_2^+ path, and the solid lines with the empty symbols correspond to the X_3^- path.

concave along the X_2^+ one, with $\text{CaCd}_2\text{Mn}_2\text{O}_7$ and $\text{CaCd}_2\text{Mn}_2\text{O}_6$ systems being an exception. On the other hand, at A-sites (purple square marks), this behaviour is reversed, *i.e.*, the relationship between V_3 and P is concave along the X_3^- path and convex along the X_2^+ one, except for the $\text{Ca}_3\text{Mn}_2\text{O}_7$ compound. Although the polarization remains unchanged along both paths, the path chosen, *via* X_2^+ or X_3^- path, for the ferroelectric transition in these materials, can have large effects on the EFG components due to the different atomic displacements caused by these distortions.

Most of the sites studied here have no inversion symmetry. This symmetry element is present only at A-sites of the $Cmce$ phase for the RP2 perovskites and at A- and A'-sites of the $Pbam$ phase for DP structures. Consequently, the inversion symmetry element at those sites cancels the linear terms in the Taylor expansion because displacements along x , y , and z axes are related, by inversion, to displacements in the opposite directions. Table 1 shows the values of the coefficients of the Taylor expansion for each $V_3 \times P$ fitting presented in Fig. 5, indicating that this relationship is always quadratic in those sites with inversion symmetry. This result was expected and agrees with that by Dening and Casabella,¹⁰ and also with the results obtained for some proper ferroelectric materials.¹⁵

On the other hand, at all sites without inversion symmetry, the linear relationship between EFG and P was not observed, as has been claimed. This behaviour could be explained by the local symmetry of these sites without inversion symmetry since they present either mirror planes or 2-fold rotation axes that are responsible for inverting x , y , or z axes direction. Therefore, the axes direction inversions should cancel some of the linear terms in the Taylor expansion, turning the first-order term very small or even null. Consequently, the second-order terms become important for fitting the data.

Additionally, because the ferroelectric transition in HIF perovskites involves a combination of octahedral rotations with linear atomic displacements, it is expected that the Taylor expansion does not converge as fast as in the proper ferroelectric materials. Nevertheless, our results show that the

quadratic relationship between the EFG V_3 component and P is dominant in the HIF materials studied in this investigation, regardless of whether the site in question has inversion symmetry or not.

4 Conclusions

We performed a first principles investigation of the spontaneous electric polarization and electric field gradient correlations in several HIF materials based on the RP phases and DP structures. The $\text{AA}_2'\text{B}_2\text{O}_7$ and $\text{AA}'\text{B}_2\text{O}_6$ structures (with A, A' = Ca, Cd and B = Mn, Ti) were analysed, focusing on A-, A'-, and B-sites.

The variations of the EFG tensor components were computed for the two possible polarization switching paths. We observed that there are interchanges among the EFG tensor components along the distortion paths at many sites, in the phase transition from the distorted to the undistorted structures. Since these interchanges are not due to the distortions, but to a swap in the EFG tensor principal axes, we used an alternative component, V_3 , suitable to be expanded in a Taylor series, allowing us to investigate the correlation between the EFG tensor proper values and the polarization P . Even considering the great complexity of the HIF compounds, the sites without inversion symmetry presented a $V_3 \times P$ correlation essentially quadratic and the claimed linear correlation between EFG and P was not observed. In some cases, quartic order terms with small coefficients had to be included in Taylor's expansion to describe V_3 as a function of the polarization properly. In turn, concerning the sites that have inversion symmetry, this correlation is always quadratic.

In addition to contributing to a fundamental understanding of the HIF perovskites' phase transitions, the P and EFG relationships also enable a deeper comprehension of macroscopic properties *via* experimental measurements of local properties. Thus, this relationship opens avenues to the analysis of

octahedral distortions that underlie HIF materials' functional multiferroic properties.

Conflicts of interest

There are no conflicts to declare.

Acknowledgements

SSMS, PRR, AMLL, and JPA acknowledge funding from the FCT projects UID/NAN/50024/2019, NECL under NORTE-01-0145-FEDER-02 2096, POCI-01-0145-FEDER-029454, and POCI-01-0145-FEDER-032527, and CERN/FIS-TEC/0003/2019. PRR also gratefully thanks the UE, FSE and FCT-Portugal for the Grant No. SFRH/BD/117448/2016. MLM, LVCA, and HMP acknowledge funding from FAPESP, Projects 2018/07760-4 and 2019/07661-9. LVCA and HMP also acknowledge support from CNPq projects 305753/2017-7 and 311373/2018-6. The authors also thank CAPES and the National Laboratory for Scientific Computing (LNCC/MCTI, Brazil) for providing HPC resources of the Santos Dumont supercomputer (<http://sdumont.lncc.br>) and PRACE for allowing them to access Marconi 100 hosted by Cineca, Italy. All this support contributed to the research results reported in this paper.

References

- G. Schatz and A. Weidinger, *Nuclear condensed matter physics: nuclear methods and applications*, Wiley, New York, NY, 1996.
- J. Schell, P. Schaaf and D. C. Lupascu, *AIP Adv.*, 2017, **7**, 105017.
- R. L. Raser and G. L. Catchen, *Ferroelectrics*, 1993, **150**, 151–161.
- B. Gao, F.-T. Huang, Y. Wang, J.-W. Kim, L. Wang, S.-J. Lim and S.-W. Cheong, *Appl. Phys. Lett.*, 2017, **110**, 222906.
- P. Rocha-Rodrigues, S. S. M. Santos, I. P. Miranda, G. N. P. Oliveira, J. G. Correia, L. V. C. Assali, H. M. Petrilli, J. P. Araújo and A. M. L. Lopes, *Phys. Rev. B*, 2020, **101**, 064103.
- P. Rocha-Rodrigues, S. S. M. Santos, G. N. P. Oliveira, T. Leal, I. P. Miranda, A. M. Dos Santos, J. G. Correia, L. V. C. Assali, H. M. Petrilli, J. P. Araújo and A. M. L. Lopes, *Phys. Rev. B*, 2020, **102**, 104115.
- T. Oja and P. A. Casabella, *Phys. Rev.*, 1969, **177**, 830–838.
- M. E. Fitzgerald and P. A. Casabella, *Phys. Rev. B*, 1970, **2**, 1350–1354.
- M. E. Fitzgerald and P. A. Casabella, *Phys. Rev. B*, 1973, **7**, 2193–2195.
- D. C. Denning and P. A. Casabella, *J. Magn. Reson.*, 1980, **38**, 277–282.
- Y. Yeshurun, Y. Schlesinger and S. Havlin, *J. Phys. Chem. Solids*, 1979, **40**, 231–237.
- O. Kanert, H. Schulz and J. Albers, *Solid State Commun.*, 1994, **91**, 465–469.
- A. M. L. Lopes, J. P. Araújo, V. S. Amaral, J. G. Correia, Y. Tomioka and Y. Tokura, *Phys. Rev. Lett.*, 2008, **100**, 155702.
- K. Choudhary, J. N. Ansari, I. I. Mazin and K. L. Sauer, *Sci. Data*, 2020, **7**, 362.
- J. N. Gonçalves, A. Stroppa, J. G. Correia, T. Butz, S. Picozzi, A. S. Fenta and V. S. Amaral, *Phys. Rev. B*, 2012, **86**, 035145.
- J. N. Gonçalves, V. S. Amaral, J. G. Correia, A. Stroppa, A. S. Fenta, A. Baghizadeh and S. Picozzi, *EPJ Web Conf.*, 2014, **75**, 09002.
- J. N. Gonçalves, V. S. Amaral, J. G. Correia, A. M. L. Lopes, J. P. Araújo and P. B. Tavares, *J. Phys. Condens. Matter*, 2014, **26**, 215401.
- G. N. P. Oliveira, R. C. Teixeira, R. P. Moreira, J. G. Correia, J. P. Araújo and A. M. L. Lopes, *Sci. Rep.*, 2020, **10**, 4686.
- F. Iwase, *Mater. Res. Express*, 2020, **7**, 025104.
- J. P. Perdew, K. Burke and M. Ernzerhof, *Phys. Rev. Lett.*, 1996, **77**, 3865–3868.
- P. Giannozzi, S. Baroni, N. Bonini, M. Calandra, R. Car, C. Cavazzoni, D. Ceresoli, G. L. Chiarotti, M. Cococcioni, I. Dabo, A. Dal Corso, S. de Gironcoli, S. Fabris, G. Fratesi, R. Gebauer, U. Gerstmann, C. Gougoussis, A. Kokalj, M. Lazzeri, L. Martin-Samos, N. Marzari, F. Mauri, R. Mazzarello, S. Paolini, A. Pasquarello, L. Paulatto, C. Sbraccia, S. Scandolo, G. Sclauzero, A. P. Seitsonen, A. Smogunov, P. Umari and R. M. Wentzcovitch, *J. Phys. Condens. Matter*, 2009, **21**, 395502.
- P. Giannozzi, O. Andreussi, T. Brumme, O. Bunau, M. Buongiorno Nardelli, M. Calandra, R. Car, C. Cavazzoni, D. Ceresoli, M. Cococcioni, N. Colonna, I. Carnimeo, A. Dal Corso, S. de Gironcoli, P. Delugas, R. A. DiStasio, A. Ferretti, A. Floris, G. Fratesi, G. Fugallo, R. Gebauer, U. Gerstmann, F. Giustino, T. Gorni, J. Jia, M. Kawamura, H.-Y. Ko, A. Kokalj, E. Küçükbenli, M. Lazzeri, M. Marsili, N. Marzari, F. Mauri, N. L. Nguyen, H.-V. Nguyen, A. Otero-de-la Roza, L. Paulatto, S. Poncé, D. Rocca, R. Sabatini, B. Santra, M. Schlipf, A. P. Seitsonen, A. Smogunov, I. Timrov, T. Thonhauser, P. Umari, N. Vast, X. Wu and S. Baroni, *J. Phys. Condens. Matter*, 2017, **29**, 465901.
- P. E. Blöchl, *Phys. Rev. B*, 1994, **50**, 17953–17979.
- R. M. Wentzcovitch, *Phys. Rev. B*, 1991, **44**, 2358–2361.
- R. M. Wentzcovitch, J. L. Martins and G. D. Price, *Phys. Rev. Lett.*, 1993, **70**, 3947–3950.
- R. D. King-Smith and D. Vanderbilt, *Phys. Rev. B*, 1993, **47**, 1651–1654.
- D. Vanderbilt and R. D. King-Smith, *Phys. Rev. B*, 1993, **48**, 4442–4455.
- H. J. Monkhorst and J. D. Pack, *Phys. Rev. B*, 1976, **13**, 5188–5192.
- M. L. Marcondes, S. S. M. Santos, I. P. Miranda, P. Rocha-Rodrigues, L. V. C. Assali, A. M. L. Lopes, J. P. Araújo and H. M. Petrilli, *J. Mater. Chem. C*, 2020, **8**, 14570–14578.
- A. Stroppa, D. Di Sante, P. Barone, M. Bokdam, G. Kresse, C. Franchini, M.-H. Whangbo and S. Picozzi, *Nat. Commun.*, 2014, **5**, 1–8.

- 31 S. Hu, H. Gao, Y. Qi, Y. Tao, Y. Li, J. R. Reimers, M. Bokdam, C. Franchini, D. Di Sante, A. Stroppa and W. Ren, *J. Phys. Chem. C*, 2017, **121**, 23045–23054.
- 32 F. Bi, S. Markov, R. Wang, Y. Kwok, W. Zhou, L. Liu, X. Zheng, G. Chen and C. Yam, *J. Phys. Chem. C*, 2017, **121**, 11151–11158.
- 33 I.-H. Park, Q. Zhang, K. C. Kwon, Z. Zhu, W. Yu, K. Leng, D. Giovanni, H. S. Choi, I. Abdelwahab, Q.-H. Xu, T. C. Sum and K. P. Loh, *J. Am. Chem. Soc.*, 2019, **141**, 15972–15976.
- 34 J. Even, L. Pedesseau, J.-M. Jancu and C. Katan, *J. Phys. Chem. Lett.*, 2013, **4**, 2999–3005.
- 35 F. Wang, H. Gao, C. de Graaf, J. M. Poblet, B. J. Campbell and A. Stroppa, *npj Comput. Mater.*, 2020, **6**, 183.
- 36 H. T. Stokes, D. M. Hatch and B. J. Campbell, *ISOTROPY Software Suite*, iso.byu.edu.
- 37 B. J. Campbell, H. T. Stokes, D. E. Tanner and D. M. Hatch, *J. Appl. Crystallogr.*, 2006, **39**, 607–614.
- 38 J. Autschbach, S. Zheng and R. W. Schurko, *Concepts Magn. Reson., Part A*, 2010, **36**, 84–126.